

## Research Article

# Thermal Stabilization of Polyoxymethylene by PEG-Functionalized Hydroxyapatite: Examining the Effects of Reduced Formaldehyde Release and Enhanced Bioactivity

Klaudia Król-Morkisz,<sup>1</sup> Ewelina Karas,<sup>1</sup> Tomasz M. Majka,<sup>2</sup> Krzysztof Pielichowski <sup>2</sup> and Kinga Pielichowska <sup>1</sup>

<sup>1</sup>AGH University of Science and Technology, Faculty of Materials Science and Ceramics, Department of Biomaterials and Composites, Al. Adama Mickiewicza 30, 30-059 Kraków, Poland

<sup>2</sup>Cracow University of Technology, Department of Chemistry and Technology of Polymers, Ul. Warszawska 24, 31-155 Kraków, Poland

Correspondence should be addressed to Kinga Pielichowska; [kingapie@agh.edu.pl](mailto:kingapie@agh.edu.pl)

Received 2 July 2019; Accepted 30 August 2019; Published 19 December 2019

Academic Editor: Leonard D. Tijing

Copyright © 2019 Klaudia Król-Morkisz et al. This is an open access article distributed under the Creative Commons Attribution License, which permits unrestricted use, distribution, and reproduction in any medium, provided the original work is properly cited.

Nanostructured hydroxyapatite (HA) functionalized with poly(ethylene glycol) (HA-g-PEG) of different molar mass was used as a thermal stabilizer to prepare polyoxymethylene (POM) composites by a melt processing method. The chemical and crystalline structure of (HA-g-PEG) and POM/HA-g-PEG composites was investigated by means of FTIR and XRD. The thermal properties, degree of crystallinity, and melting behaviour of POM-based composites were analysed with TG, DSC, and TOPEM DSC methods. The tensile strength, Young's modulus, toughness, and wettability of POM were investigated as well. A preliminary assessment of bioactivity, *in vitro* chemical stability, and formaldehyde release from POM/HA-g-PEG composites by Schiff's test was also performed. An SEM/EDX method was used to observe the morphology of POM/HA-g-PEG composites. The results indicate that the addition of 1% HA-g-PEG slightly increases the melting temperature and degree of crystallinity. In small amounts, HA-g-PEG particles probably act as nucleating agents for the POM crystallization process. Incorporation of 5% HA-g-PEG to POM caused a decrease in the crystallinity of the polymer matrix, as a result, some mechanical properties of POM/HA-g-PEG composites also decreased. The thermal stability of POM/HA-g-PEG composites improved significantly from 309°C for unmodified POM to 342°C for POM/10.0% HA-g-PEG 600. The most effective thermal stabilizer was synthesized with the lowest mass-average molar mass PEG. The *in vitro* bioactivity test confirmed that, as the average molar mass of PEG in HA-g-PEG hybrids increased, POM-based composites indicated higher bioactivity. The *in vitro* chemical stability analysis results showed that both the POM matrix and the HA-g-PEG additive remain stable during the whole incubation time. Importantly, after seven days of dynamic incubation, no formaldehyde was detected in all filtrates, which is crucial in biomedical applications, among others.

## 1. Introduction

Polyoxymethylene (POM), also known as acetal resin or polyformaldehyde, is an engineering polymer with a vast spectrum of applications that require high tensile strength and hardness, low coefficient of friction, and excellent dimensional stability [1, 2]. It has been used in different areas, including the automotive and mechanical industries, electronics, consumer goods, home appliances, and also in medical technology as a surgical implant material and in medical devices and drug

delivery systems [3]. POM's molecular structure consists of a repeating carbon-oxygen linkage  $[-CH_2-O-]_n$  [4]. Acetal that exclusively contains the carbon-oxygen (C-O) bonds in the backbone chain is called a POM homopolymer in contrast to a POM copolymer where some comonomer units  $(CH_2-CH_2-O)$  occur in the main chain [5]. POM copolymer has increased thermal and chemical stability, but a lower degree of crystallinity due to the C-C bond presence. Therefore, its mechanical strengths, hardness, rigidity, and melting temperature are slightly lower than for POM homopolymer [6, 7].

POM homopolymer is based on the polymerization of 1,3,5-trioxane, whereas POM copolymer is manufactured by the copolymerization of 1,3,5-trioxane with cyclic ethers e.g., 1,3-dioxolane or ethylene oxide [8]. POM can be processed using all methods applicable to thermoplastics, such as extrusion, injection-moulding, and blow-moulding [9].

Despite very good mechanical and tribological properties [10, 11], POM exhibits poor thermal stability due to fast, unstoppable thermal depolymerisation reactions [12, 13]. A certain amount of formaldehyde can be released from the overheated material [6, 14]. As a result, its range of applications, in particular those in contact with living tissue, is strongly limited. To increase the thermal stability of POM different methods can be used. The stability of POM can be improved by copolymerisation to obtain C-C linkages at the expense of partial mechanical strength loss. Another method is capping the end groups of POM chains by esterification or etherification. Antioxidants, formaldehyde scavengers, and other thermal stabilizers can also be added to the POM [15, 16].

Some attempts towards POM thermal stability enhancement have been described in the literature. For example, Hu et al. [17] studied the influence of polyamide (PA) and melamine (MA) complexes on the thermal stabilization of POM copolymer. They found that the complex stabilizer PA/MA is more efficient than the use of these formaldehyde scavengers separately. The thermal stability of POM was about 274.8°C ( $T_{5\%}$ ) with PA/MA in the ratio of 0.4/0.04 wt.%. Wacharawichanant et al. [18] investigated the effect of zinc oxide (1–8 wt.%) on the thermal properties of POM. They observed a significant increase in the thermal stability of POM, as much as 20°C ( $T_{5\%} = 320.0^\circ\text{C}$  for 6 wt.% ZnO). Zhao et al. [19] manufactured a new kind of POM copolymer, based on trioxane and styrene oxide or dioxolane, with improved thermal stability. They found that 0.6 mol% styrene oxide comonomer can substantially improve the thermostability of POM ( $T_{5\%} = 191.74^\circ\text{C}$ ). However, the styrene oxide presence in the POM structure results in a decrease of crystallinity. Consequently, the mechanical strength of the new POM copolymer was also impaired.

Improvement of POM thermal stability was also observed by Meri et al. [20] in POM nanocomposites containing ethylene octene copolymer (EOC) and plasma synthesized tetrapod shaped zinc oxide (ZnO).

POM has been widely used in different long-term orthopaedic applications like hip and knee prostheses [21]. To improve biocompatibility and bioactivity of POM-based implants POM/HA nanocomposites have been investigated in our previous works [22] because hydroxyapatite ( $[\text{Ca}_{10}(\text{PO}_4)_6(\text{OH})_2]$  (HA)) is a bioceramics which is chemically similar to human inorganic hard tissue [23] and can be easily modified by functionalization [24, 25]. However, the main problem of POM/HA nanocomposites was the degradation of POM matrix in the presence of HAp during melt processing. To improve POM thermal stability and to enable incorporation of larger amounts of HA, we decided to modify HA by the grafting process of PEG on its surface using diisocyanate as a coupling agent. Using such modification hydroxyl groups on HA surface have been replaced by urethane groups linked to PEG, and catalytic activity of hydroxyl groups on POM decomposition

process has been reduced [26]. Using such modification it is possible to incorporate higher amounts of HA to POM matrix making them more bioactive than unmodified POM, that is highly desired for long-term bone implants.

In our previous study (Pielichowska et al. [25]) we used chemically modified hydroxyapatite (HA) as a thermal stabilizer for POM copolymer. HA was functionalized with poly (ethylene glycol) (PEG) with a molar mass of 2000 and 1, 6-hexamethylene diisocyanate (HDI) as a coupling agent in an HA : HDI : PEG molar ratio of 2 : 2 : 1 and incorporated into the POM matrix by the extrusion method. The thermal stability of POM was increased by 19°C ( $T_{5\%} = 347^\circ\text{C}$ –1 wt.% HA-g-PEG 2000) and 32°C ( $T_{5\%} = 360^\circ\text{C}$ –5 wt.% HA-g-PEG 2000). Now we investigate the influence of the molar mass of PEG (600, 2000, and 6000) under the HA : HDI : PEG molar ratio of 1 : 2 : 1 on the effectiveness of HA-g-PEG hybrids as thermal stabilizers for POM copolymer and on the other properties of composites, especially those related to further biomedical applications.

## 2. Experimental

**2.1. Materials.** POM copolymer Ultraform® (MFR2.6 g/10 min), average molar masses  $M_n = 8269$  and  $M_w = 78565$  ( $M_w/M_n = 8.96$ ), was produced by BASF (Germany). HA ( $\text{Ca}_{10}(\text{PO}_4)_6(\text{OH})_2$ ) nanopowder (nanoparticle size below 100 nm—99% of particles Ca/P ratio 1.67) was manufactured by nGimat Co. (USA). 1, 6-hexamethylene diisocyanate (HDI), poly (ethylene glycol) (PEG) with a mass-average molar mass of 600, 2000, 6000, and dibutyltin dilaurate (DBTDL) were products of Sigma Aldrich. Anhydrous N, N-dimethyleformamide (DMF) and ethanol were purchased from Avantor (Poland). PEG was dried under vacuum at 90°C for 24 hours before use and HA was dried at 110°C for 24 h.

**2.2. Grafting Process of HA-g-PEG and Processing of POM/HA-g-PEG Composites.** The grafting process via a two-step addition reaction, and processing of POM with HA-g-PEG additive through twin-screw extrusion/injection moulding, were performed according to the procedure described in ref. [25] and as it is presented in Figure 1. Molar ratio of substrates HA:HDI:PEG was 1:2:1 (Table 1) to keep the balance between the inorganic HA filler and the biocompatible PEG component. Samples containing 0, 0.5, 1.0, 2.5, 5, and 10.0% w/w of HA-g-PEG (calculated in relation to pristine HA) have been obtained in dumbbell shape.

**2.3. Techniques.** Fourier transform infrared (FTIR) spectra of POM/HA-g-PEG composites and HA-g-PEG powders were taken using an HATR PIKE attachment with diamond crystal and in KBr pellets, respectively, and a Bruker Vertex 70 V FTIR spectrometer. All measurements were performed in the range of 4000–400  $\text{cm}^{-1}$  with 2  $\text{cm}^{-1}$  resolution at room temperature.

Wide angle X-ray diffraction (WAXD) experiments were performed at room temperature using a Philips X'Pert Pro MD diffractometer with monochromatic  $\text{CuK}\alpha_1$  radiation monochromatized by Ge (111) monochromator. Data were collected in Bragg–Brentano geometry with a  $2\theta$  scanning

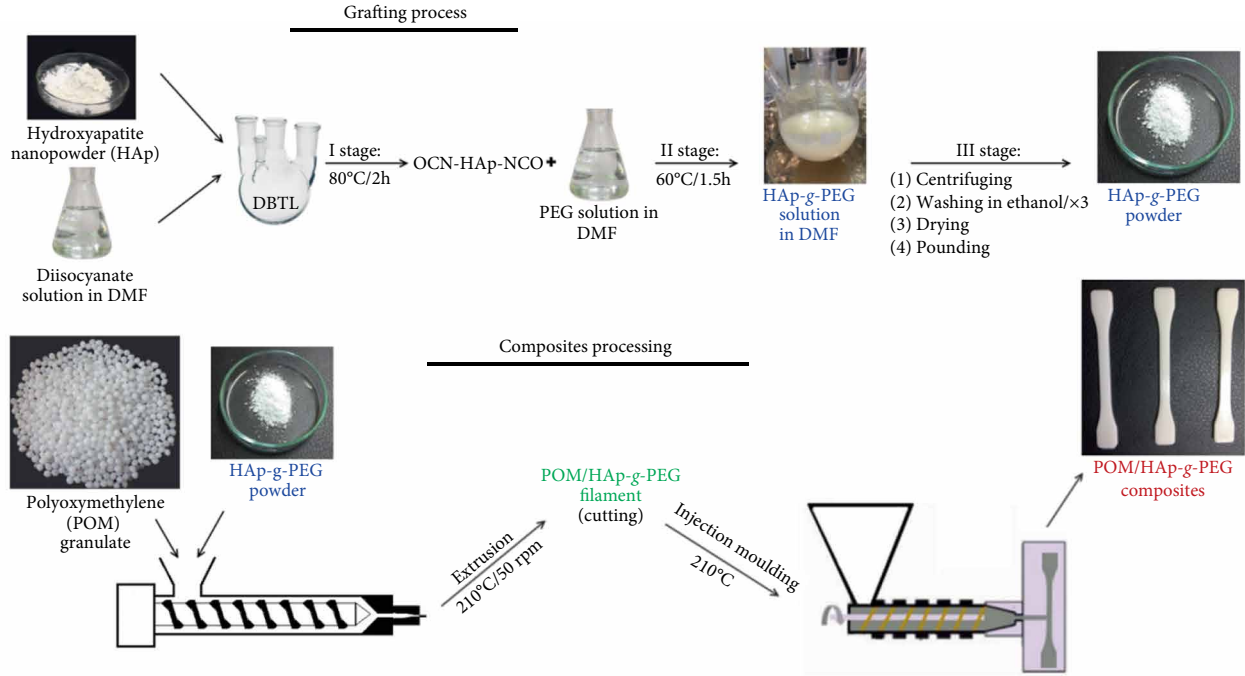


FIGURE 1: Preparation of POM/HA-g-PEG composites.

TABLE 1: Composition of HA-g-PEG systems.

Sample	HA [g]/DMF [ml]	HDI [ml]/DMF [ml]	PEG [g]/DMF [ml]
HA-g-PEG 600	9.0/90	6/12	10.8/11
HA-g-PEG 2000	9.0/90	6/12	36.0/36
HA-g-PEG 6000	9.0/90	6/12	108.0/108

range from 15–60° and 0.008° step size. The degree of crystallinity [ $X_c$ ] for HA and HA-g-PEG systems were calculated using the equation:

$$X_c = \frac{I_{300} - V_{112/300}}{I_{300}}, \quad (1)$$

where:  $X_c$  [%] is the degree of crystallinity of HA,  $I_{300}$  is the intensity of (300) diffraction peak, and  $V_{112/300}$  is the intensity of the hollow between (112) and (300) diffraction peaks of HA [27]. The crystal size of HA and HA-g-PEG systems was calculated using a Debye–Scherrer equation:

$$D = \frac{K \cdot \lambda}{\beta \cdot \cos(\theta)}, \quad (2)$$

where:  $D$  [nm] is the particle size,  $K$  is the broadening constant ( $K = 0.9$ ),  $\lambda$  is the wavelength of  $\text{CuK}\alpha$  radiation ( $\lambda = 0.15406\text{nm}$ ),  $\beta$  is the peak width at half height,  $\theta$  represents the peak position. The crystallite size was measured for the (002) reflection peak because this Miller index corresponds to the  $c$ -axis length [28].

DSC curves were recorded using a DSC1 (Mettler-Toledo) operating in dynamic mode. DSC measurements were performed in accordance with ISO 11357-3:2009. The samples (~5 mg each) were placed in 40  $\mu\text{l}$  pierced aluminium pans.

An empty pan was used as a reference. A heating/cooling rate of 10 K/min and a nitrogen atmosphere (flow of 30 ml/min) were applied. The degree of crystallinity ( $X_c$ ) of each sample, calculated in relation to pure POM, was determined using Equation (3):

$$X_c = \frac{\Delta H_m}{(1-w) \times \Delta H_m^0} \times 100\%, \quad (3)$$

where:  $\Delta H_m^0$  is the heat of fusion determined from the DSC curves,  $\Delta H_m$  is the heat of fusion of 100% crystalline POM ( $\Delta H_m^0 = 326.3\text{J/g}$ ) [29] and  $w$  is the weight fraction of HA-g-PEG in the POM composites.

The temperature-modulated differential scanning calorimetry with stochastic temperature modulations (TOPEM-DSC, Mettler-Toledo) was also applied. The conditions for TOPEM measurements were: 1 K amplitude, 15–30 s switching time, and 2 K/min underlying heating rate.

TG measurements were carried out on a Netzsch STA 449 Jupiter thermogravimetric analyser at a 10 K/min heating rate in a nitrogen atmosphere (50 ml/min  $\text{N}_2$  gas flow rate). The temperature range was 25–600°C. The samples (ca. 8 mg) were placed in  $\text{Al}_2\text{O}_3$  crucibles. From the TG curves, the temperatures of 3, 5, 10, 20, and 50% mass loss were determined ( $T_{x\%}$ —where  $x$  is percent of mass loss).

The tensile tests were performed on a Zwick-Roell universal testing machine with a 50 mm/min crosshead speed (according to ISO 527) at room temperature. Injection moulding technique was applied to shape the samples for tensile testing according to ISO 3167 standard. Three samples in the shape of a dumbbell (1.97 mm  $\pm$  0.02 mm in thickness and 4.85 mm  $\pm$  0.05 mm in width) were tested for each composite composition. Values of Young's modulus ( $E$ ) and ultimate tensile strength ( $R_m$ ) were taken from stress-strain profiles. On

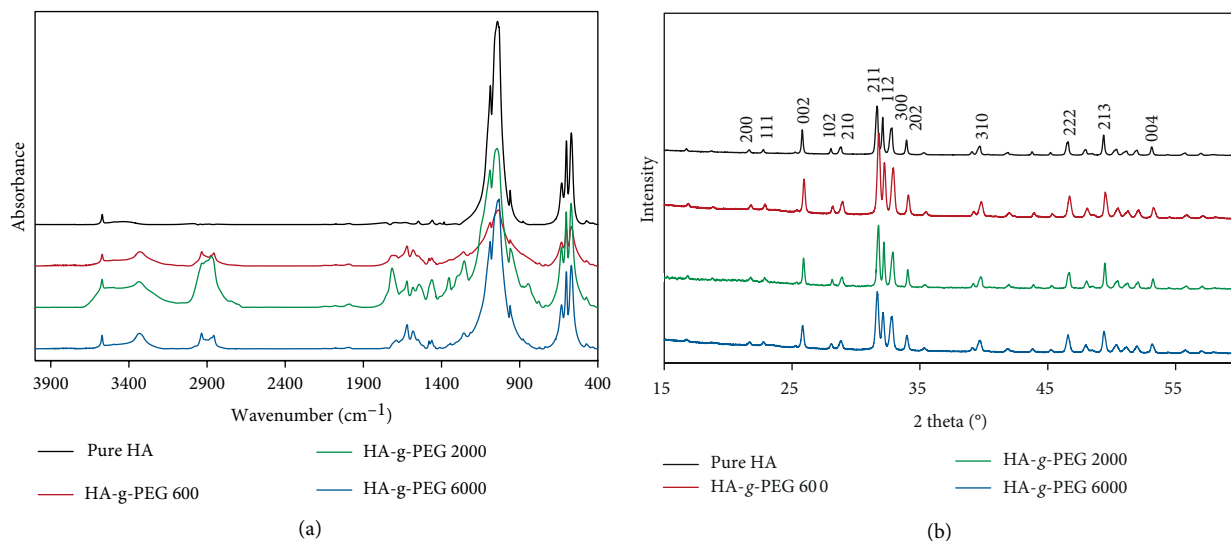


FIGURE 2: FTIR spectra (a) and XRD patterns (b) of HA and HA-g-PEG.

the basis of the area under the stress–strain curve, in accordance with Equation (4), the toughness, as the amount of energy that was absorbed per unit volume (energy density) of material until break, was calculated.

$$E = \int_0^{\varepsilon_f} \sigma \cdot d\varepsilon, \quad (4)$$

where:  $E$  is the energy density,  $\varepsilon_f$  is the strain at fracture,  $\varepsilon$  is strain, and  $\sigma$  is stress.

The water contact angles of sample surfaces were measured on a DSA 10MK2 (Kruss, Germany) contact angle goniometer by the sessile drop method at ambient temperature.  $0.2 \mu\text{l}$  ultra-high quality (UHQ) deionized water droplets were put on the sample surface. Ten data points were collected at ten different positions on the sample surface and the average values were calculated.

The microstructure of the composites was observed using a FEI Nova Nano SEM 200 scanning electron microscope (SEM) equipped with energy dispersive X-ray (EDX) analyser (EDAX Company) at 5 kV electron beam energy. All samples were coated with a carbon layer just before the measurement.

POM/HA-g-PEG composites were soaked in a 1.5x concentrated simulated body fluid (SBF) at  $37^\circ\text{C}$  for 21 days; the sample mass to SBF volume ratio was 1 : 10. The SBF solution was changed every 3 days. Then, the samples were removed from the SBF, softly rinsed with distilled water, and dried. After SBF incubation, the sample surface was examined by SEM-EDX.

Unmodified POM and POM/HA-g-PEG 600 specimens were incubated at  $37^\circ\text{C}$  according to EN ISO 10993:13 for 12 weeks in Ringer fluid (RF) and phosphate-buffered saline (PBS) solutions. The pH, conductivity, and mass changes were assessed during the incubation.

Schiff's reagent was applied to detect formaldehyde release from POM/HA-g-PEG 600 composites during the incubation in distilled water at  $37^\circ\text{C}$  for 4 weeks. The sample mass to water volume ratio was 1 : 10. The water was changed every 24 h and

TABLE 2: Crystallinity [ $X_c$  [%]] and crystal size [ $D$  [nm]] of HA and HA-g-PEG systems based on XRD characterization ( $\beta$ —the peak width at half height [rad]).

Sample	$X_c$ [%]	$\beta$ [rad]	$2\theta$ [rad]	$D$ (002) [nm]
HA	87.35	0.0040	0.4503	35.43
HA-g-PEG 600	76.57	0.0035	0.4527	40.76
HA-g-PEG 2000	84.51	0.0030	0.4521	47.95
HA-g-PEG 6000	71.87	0.0037	0.4506	38.44

Schiff's test was performed after 1, 21, and 28 days. During Schiff's test, the water was decanted into test tubes, 3 drops of Schiff's reagent were added to every test tube and the solutions were mixed well. Distilled water was used as a reference sample. The changes in the solutions' colour were monitored and photographed.

### 3. Results and Discussion

**3.1. FTIR and XRD Analysis of HA-g-PEG.** The chemical structure and functional groups of pristine HA and HA-g-PEG systems were analysed using FTIR spectroscopy. The FTIR spectra of HA and HA-g-PEGs are shown in Figure 2(a). In the FTIR spectrum for unmodified HA, the bands at  $3571 \text{ cm}^{-1}$  and  $632 \text{ cm}^{-1}$  are associated with O-H groups stretching and the liberation vibrations of HA nanoparticles, respectively. A broad band in the  $3550\text{--}3250 \text{ cm}^{-1}$  range is related to absorbed water in the sample. Absorption bands at  $1150\text{--}900 \text{ cm}^{-1}$  and  $620\text{--}500 \text{ cm}^{-1}$  are due to the vibration of  $\text{PO}_4^{3-}$  groups. For all HA-g-PEG systems absorption bands at  $3330 \text{ cm}^{-1}$ , connected with the N-H urethane stretching vibration, is observed [30]. There are also two absorption bands from  $\text{CH}_2$  groups at about  $2930$  and  $2860 \text{ cm}^{-1}$ . The absorption bands at  $1725$  and  $1630 \text{ cm}^{-1}$  are due to the vibration of C=O (carbonyl) groups in urethane bonds (I amide absorption band). The band at around  $1585 \text{ cm}^{-1}$  corresponds with N-H stretching vibration

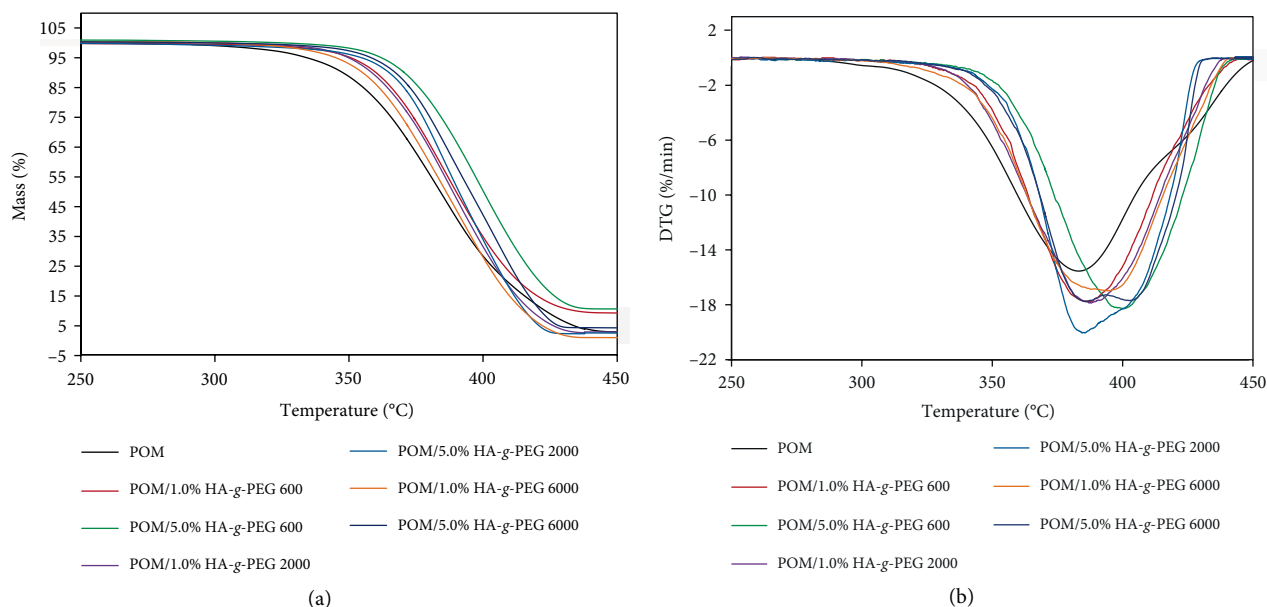


FIGURE 3: TG (a) and DTG (b) curves of POM/HA-g-PEG composites.

in urethane groups (II amide absorption band). The band at  $1253\text{ cm}^{-1}$  is consistent with C-N stretching vibrations (II amide absorption band) [31, 32]. The bands in the  $1150\text{--}950\text{ cm}^{-1}$  range from the ether C-O-C groups from PEG [33] are covered with bands related to  $\text{PO}_4^{3-}$  groups from HA [34], but the bands in this range are broader than for pristine HA.

For all HA-g-PEG samples, all components of the urethane bond are visible in the FTIR spectrum in accordance with the literature [35]. The lack of an  $\text{-N=C=O}$  (isocyanate) absorption band at about  $2260\text{ cm}^{-1}$  confirmed a total conversion of HDI with  $\text{-OH}$  groups; as a result, urethane bonds ( $\text{-NH-CO-O-}$ ) were created. Based on the obtained results, it can be assumed that the grafting process of PEG using HDI as a coupling agent has been successfully performed.

Additionally, the XRD diffraction measurements for pure HA and HA-g-PEG were performed and the results are shown in Figure 2(b). The XRD pattern of pure HA includes all characteristic peaks corresponding to stoichiometric HA [36]. The diffractograms of all HA-g-PEG samples did not reveal any extra peaks. However, as compared to pure HA, the HA-g-PEG's diffraction peaks were slightly out of phase and the size of peaks was subtly changed. Data from XRD patterns were recalculated using Equations (1) and (2) to yield crystallinity of samples and the crystal size of HA—Table 2.

The crystallinity of HA was reduced for all modified samples by up to 15.48% for HA-g-PEG 6000. The crystal size of modified samples increased from 8.5% (for HA-g-PEG 6000) to 35% (for HA-g-PEG 2000). These results suggest that the grafting process of PEG on the HA surface strongly affects the crystallographic structure of stoichiometric HA. The unit cell size of modified HA was expanded, but there were no extra crystallographic planes in the HA unit cells. Considering the crystal size of the HA-g-PEG samples, the results proved that the modified HA still remains in the form of nanoparticles. Similar effects were observed by Li et al. [37] where after modification of HA by strontium a decrease in the HA crystallinity

and expansion of crystal size have been observed. In case of HA-g-PEG, such effects can be connected to incorporation of polymer chains to HA crystal lattice. In HA-g-PEG systems, the amount of organic phase (as determined from TG) was 22.3, 24.1, and 17.1% for PEG 600, 2000, and 6000, respectively. Such results suggest that smaller amounts of chemically surface-bonded polymer chains allows other chains to be incorporated into HA structure, while larger amounts of polymer chains on HA surface hinder further incorporation and, in consequence, changes in HA diffraction parameters are lower.

**3.2. TG/DTG Studies of POM/HA-g-PEG Composites.** The thermal stability of POM/HA-g-PEG composites was investigated using TG methods, and TG and DTG (first derivative of TG) curves are shown in Figure 3. In addition, characteristic temperatures of weight loss ( $T_{1-50\%}$ ) and  $T_{DTGmax}$  are presented in Table 3.

In comparison to pristine nanohydroxyapatite (nHA), which strongly catalyses the thermal decomposition of POM by up to  $30^\circ\text{C}$  [22], the addition of HA grafted with PEG (HA-g-PEG) contributed to the significant improvement of POM thermal stability, similar to what was observed for HA functionalized with a molar ratio 2:2:1. HA contains in its structure both acid and basic sites in a single crystal lattice [38–40]. In our studies, stoichiometric HA has been applied with molar ratio of Ca/P 1.67. It is known from literature that stoichiometric HA possesses mainly basic sites [41]. On the other hand, POM is very sensitive to heat and in the presence of acids and bases easily undergoes depolymerisation to formaldehyde. In the functionalization reaction of HA we have performed, the number of basic active sites on HA surface has been reduced by the reaction between HA hydroxyl groups and isocyanate groups with formation of urethane groups. Additionally, urethane bonds that were formed contain nitrogen atoms just like other commercially available POM heat

TABLE 3: Thermal stability of POM/HA-g-PEG composites.

Sample	$T_{3\%}$ [°C]	$T_{5\%}$ [°C]	$T_{10\%}$ [°C]	$T_{20\%}$ [°C]	$T_{50\%}$ [°C]	$T_{DTG}$ [°C]
POM*	319.0	328.1	341.2	355.1	382.0	388.1
POM/1.0% HA-g-PEG 600	343.8	351.0	360.3	370.4	390.0	387.0
POM/5.0% HA-g-PEG 600	351.9	359.8	369.4	379.8	399.6	401.3
POM/10.0% HA-g-PEG 600	356.7	365.2	376.0	386.6	405.9	402.0
POM/1.0% HA-g-PEG 2000	343.0	349.3	358.3	368.8	388.7	387.0
POM/5.0% HA-g-PEG 2000	344.9	354.6	365.0	374.4	391.1	384.5
POM/10.0% HA-g-PEG 2000	342.9	354.8	367.2	377.8	395.5	387.5
POM/1.0% HA-g-PEG 6000	334.8	343.6	354.6	365.4	385.9	391.3
POM/5.0% HA-g-PEG 6000	347.2	356.8	366.3	376.2	394.9	389.2
POM/10.0% HA-g-PEG 6000	341.9	351.8	363.5	375.4	396.5	405.0

\*Data for unmodified POM were taken from Ref. [25].

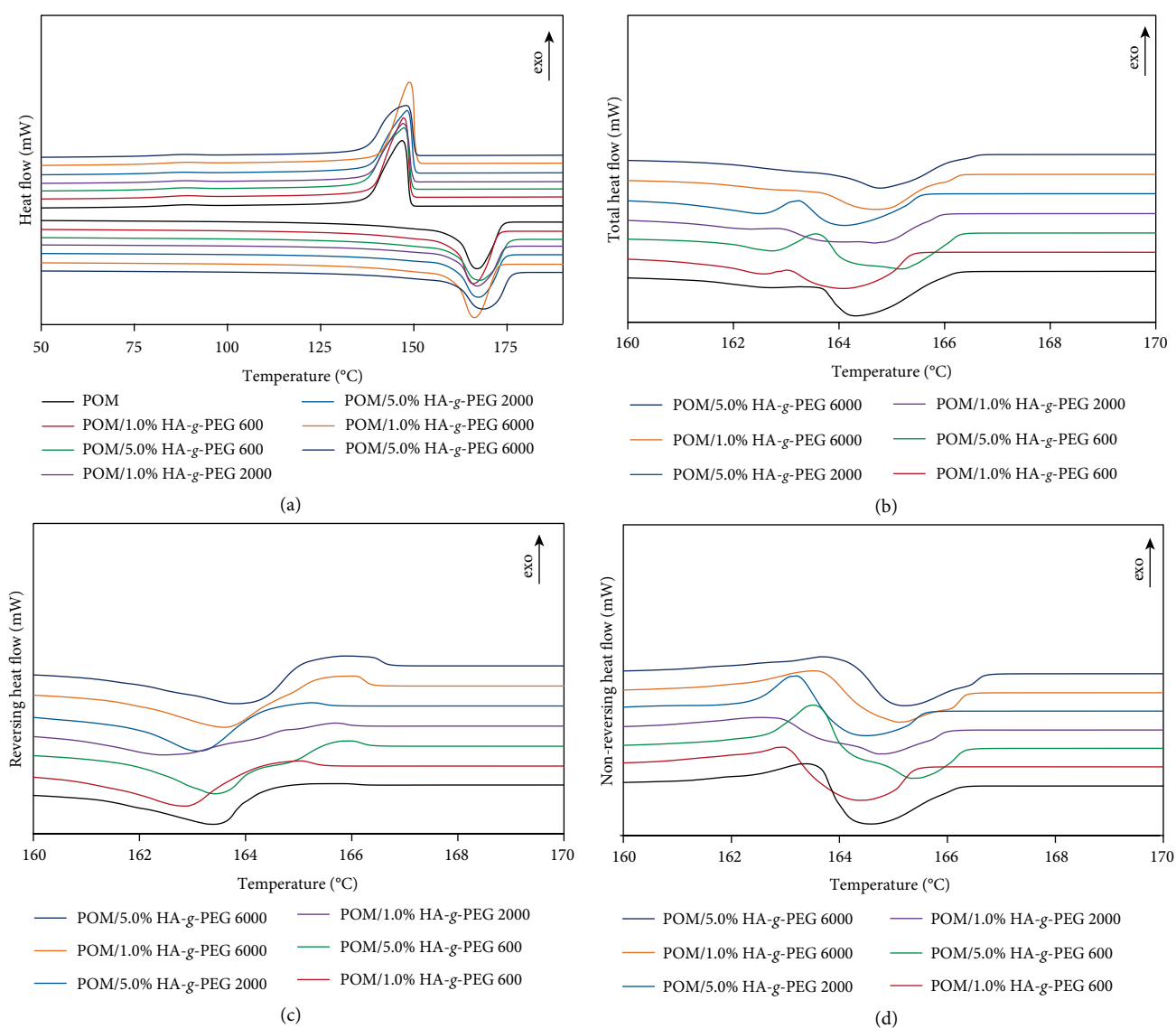


FIGURE 4: DSC curves (a) (the second heating run) and TOPEM-DSC profiles (b-d) of POM/HA-g-PEG composites.

stabilizers, such as polyamides, aromatic amines, and dicyandiamines [8]. In consequence, reduction in the number of hydroxyl groups and incorporation of nitrogen atoms lead to remarkable improvements in POM thermal stability that broadens the application field of this important engineering polymer.

As seen in the TG data, for 3% HA-g-PEG in POM composites, a thermal stability improvement ( $T_{3\%}$ ) from 15.8°C for 10% HA-g-PEG 2000 to 37.7°C for 10% HA-g-PEG 600 was observed. Generally, for HA functionalized with PEG 2000 at a molar ratio of 2:2:1, improvement in thermal stability was higher (ca. 30°C for 10% HA-g-PEG 2000 [25]) compared to HA functionalized with a molar ratio of 1:2:1, where improvement in thermal stability was 23.9°C for 10% HA-g-PEG 2000. However, the best results were found for HA functionalized with PEG 600 at a molar ratio of 1:2:1. A strong relationship between the average molar mass of PEG and the efficiency of HA-g-PEG additive was observed. The shorter the chains of PEG used, the higher the thermal stability of the POM composites was achieved. This effect is probably the result of the higher PEG chain mobility that leads to a more efficient grafting process and reduction of hydroxyl groups in HA by the reaction of -OH groups with isocyanate groups from HDI with the formation of urethane bonds on the HA surface. Moreover, in the synthesis reaction of HA-g-PEG, when PEG of lower molar mass (600) is used, the mixture is less viscous due to a modest amount of PEG (see Table 1) and the PEG chains are more mobile. Therefore, they can more easily react with other compounds and more -OH groups can be substituted—as a result, the HA-g-PEG thermal stabilizer is more effective. Thus, the effect of heat stabilization by nitrogen-containing HA-g-PEG can be intensified.

**3.3. DSC and TOPEM-DSC Results of POM/HA-g-PEG Composites.** POM/HA-g-PEG composites, that were manufactured using melt processing techniques such as extrusion and injection moulding, were characterized by DSC (Figure 4(a)). Temperatures of phase transitions (1st and 2nd melting, crystallization) and the values of the corresponding heat of phase transition are collected in Table 4. Based on the DSC results, the degree of crystallinity of the POM matrix in composites and supercooling of composites was calculated and correlated in Table 4.

There is very little impact of HA-g-PEG additives on the shape of DSC curves, the melting point temperature, the degree of crystallinity, and supercooling. Moreover, no significant influence of PEG average molar mass on the phase behaviour of POM composites was observed. Additionally, when comparing the obtained results to results of POM/HAp-g-PEG 2000 grafted at the HAp:HDI:PEG molar ratio of 2:2:1 [25], no influence of substrate ratio on melting and crystallization behaviour of POM composites can be found. The melting temperature of POM/HA-g-PEG composites decreased by 1–2°C, except for POM/1.0% HA-g-PEG 600, where an increase of 1.5°C was detected. For the second melting run, the melting temperature decreased by ca. 0.3–0.8°C. The addition of HA-g-PEG in composites alters the crystallinity of the POM matrix (a decrease of 1%). Only for the composite

containing 1% HA-g-PEG 6000 was an increase of 0.8% in POM crystallinity detected. Furthermore, a slight decrease by ca. 1–3°C of supercooling of all composites was observed, which confirms the nucleating effect of additives on POM crystallization. There was a lack of melting peak in the range 15–70°C corresponding to PEG melting for all three PEG components. This indicates that PEG was chemically bonded in an organic–inorganic HA-g-PEG compound, so the mobility of PEG chains was strongly limited and as a result, PEG crystallization was hindered. There was only one maximum in the melting peak, both in the first and second runs in contrast to our previous study, where pure HA was added to the POM matrix [22]. This can indicate that HA-g-PEG systems affect the lamellar thickness of POM crystals.

To obtain more information about the thermal behaviour of POM/HA-g-PEG composites TOPEM DSC was applied. TOPEM DSC profiles (total heat flow is presented in Figure 4(b)) were separated to reversing (Figure 4(c)) and nonreversing (Figure 4(d)) heat flow. As it can be seen from the TOPEM DSC traces, melting transitions, are found at significantly lower temperatures than those of the classical DSC. This phenomenon was also observed by other researchers [42] and can be attributed to lower heating rates that are required in modulated DSC measurements. For unmodified POM, one melting peak is visible in total heat flow, whereas on the nonreversing curve, a minor exothermic peak ascribed to the recrystallization of less ideal POM crystals can be observed. For composites containing HA-g-PEG, a double melting peak in the total heat flow curve is present. It can be clearly seen that maximum melting peak depends both on the PEG average molar mass and HAp-g-PEG content. With an increase in PEG molar mass and HA-g-PEG content, the maximum peaks were shifted to higher temperatures, and the highest temperatures were observed for POM modified with 5% of HA-g-PEG 6000. This effect can be attributed to the highest crystallization ability of PEG 6000 compared to PEG with lower molar mass, and better affinity of longer PEG chains to embed in the crystal structures of POM. This can be confirmed by the lower recrystallization effect for composites with HA-g-PEG 6000 in TOPEM nonreversing heat flow profiles and the highest degree of crystallinity of POM/HA-g-PEG 6000 composites. Along with an HA-g-PEG content increase, a stronger recrystallization effect and complete melting processes are detected in nonreversing curves, especially for 5% HA-g-PEG 600 and HA-g-PEG 2000. The two melting peaks are probably associated with melting of dysfunctional POM crystals that were disturbed by HA-g-PEG with shorter PEG chains. Similar effects were observed for polyurethane (MDI-PEG-BDO) samples modified with graphite nanofiller [43].

**3.4. XRD and FTIR-ATR Results of POM/HA-g-PEG Composites.** Figure 5 show the XRD patterns of unmodified POM, POM/1.0%HA-g-PEG, and POM/5.0%HA-g-PEG composites.

As can be seen, for all samples there are five characteristic XRD peaks that are located at  $2\theta$  of approximately 22.8°, 34.3°, 40.0°, 48.0°, and 53.8°. These peaks were assigned to (100),

TABLE 4: Temperature, heat of melting, supercooling, and degree of crystallinity of POM/HA-g-PEG composites (during first heating and second heating cycles).

Sample	$T_{max}$ [°C]	Heat of phase transition of POM/HA-g-PEG [J/g]	POM heat of melting [J/g]	Supercooling [°C]	Degree of crystallinity [%]
POM	165.8	159.5	159.5	19.1	48.9
POM/1.0% HA-g-PEG 600	168.5	159.6	159.6	21.2	49.4
POM/5.0% HA-g-PEG 600	166.5	150.9	150.9	18.0	48.7
POM/1.0% HA-g-PEG 2000	166.3	157.7	157.7	19.1	48.3
POM/5.0% HA-g-PEG 2000	168.5	149.2	149.2	20.3	47.0
POM/1.0% HA-g-PEG 6000	167.5	158.9	158.9	18.7	49.0
POM/5.0% HA-g-PEG 6000	165.8	149.8	149.8	17.8	48.4
POM	167.0	170.9	170.9	20.3	52.4
POM/1.0% HA-g-PEG 600	167.6	166.7	166.7	20.2	51.6
POM/5.0% HA-g-PEG 600	167.4	160.2	160.2	18.9	51.7
POM/1.0% HA-g-PEG 2000	167.0	169.9	169.9	19.7	52.6
POM/5.0% HA-g-PEG 2000	167.3	159.7	159.7	19.1	51.5
POM/1.0% HA-g-PEG 6000	166.2	171.8	171.8	17.4	53.2
POM/5.0% HA-g-PEG 6000	168.5	160.3	160.3	20.5	51.7

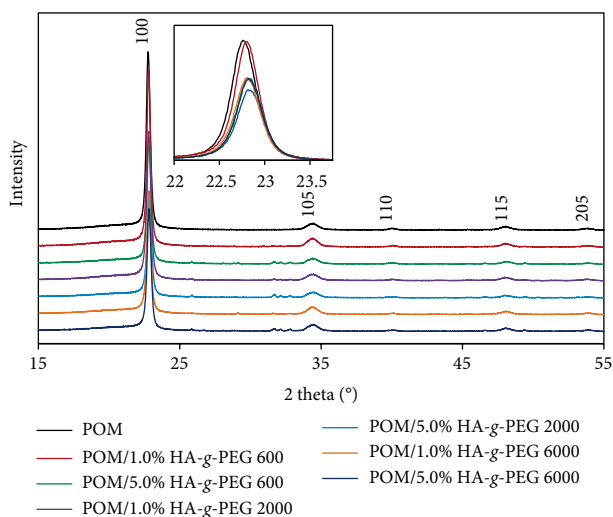


FIGURE 5: The XRD patterns of POM/HA-g-PEG composites in the range of  $2\theta = 15\text{--}55^\circ$  (a) and  $2\theta = 22\text{--}24^\circ$  (b).

(105), (110), (115), and (205) reflections of POM hexagonal crystals, respectively. The crystal structure of all samples was confirmed with XRD and it was consistent with XRD patterns for POM that are available in the literature [9, 44, 45]. For composites containing 5% of HA-g-PEG, peaks derived from HA start to show up at  $25.9^\circ$  (002),  $29.2^\circ$  (210),  $31.7^\circ$  (211),  $32.1^\circ$  (112),  $32.8^\circ$  (300),  $46.5^\circ$  (222), and  $49.5^\circ$  (213) which is in accordance with XRD patterns for HA-g-PEG (Figure 2(b)). In Figure 5, the diffraction intensity of the (100) plane is plotted closely. Both HA-g-PEG content and the molecular mass of PEG influence the size of this peak by decreasing its intensity. This indicates that the crystallinity of POM composites decreases as the amount of modifier increases and the molar mass of PEG that was used in the HA-g-PEG system increases, which is consistent with the DSC results (Table 4). The

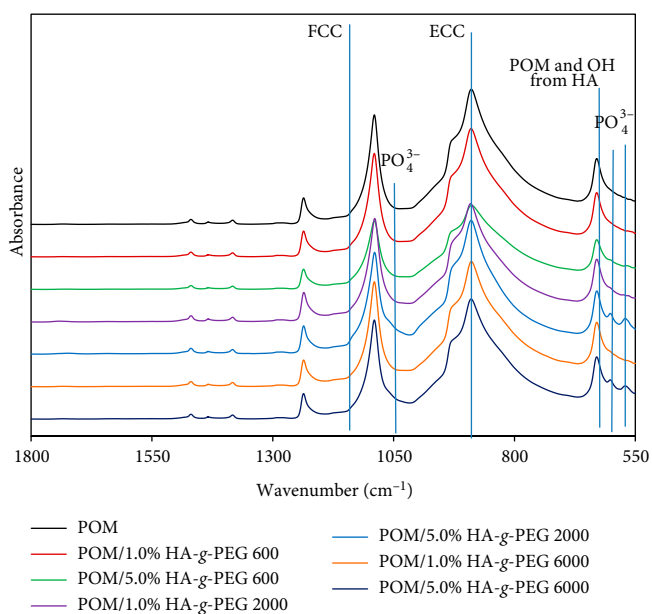


FIGURE 6: FTIR-ATR spectra of POM/HA-g-PEG composites.

FTIR-ATR spectra and the second derivative of the FTIR-ATR spectra of POM/HA-g-PEG composites are presented in Figure 6.

The group of two bands at  $2981\text{ cm}^{-1}$  and  $2923\text{ cm}^{-1}$ , that are not included in Figure 6, arises from symmetric stretching vibrations ( $\nu$ ) of  $\text{CH}_2$  groups. The band at  $1469\text{ cm}^{-1}$  is attributed to  $\text{CH}_2$  bending vibrations ( $\delta$ ). The  $1383\text{ cm}^{-1}$  band is assigned to the wagging of  $\text{CH}_2$  groups. The medium band at  $1236\text{ cm}^{-1}$  can be ascribed to the twisting of  $\text{CH}_2$  groups. The strong absorption bands at  $1089\text{ cm}^{-1}$  and  $891\text{ cm}^{-1}$  and the weak band at  $1136\text{ cm}^{-1}$  are attributed to the asymmetric stretching and the band at  $933\text{ cm}^{-1}$  is due to the symmetric stretching of C-O-C groups. The O-C-O

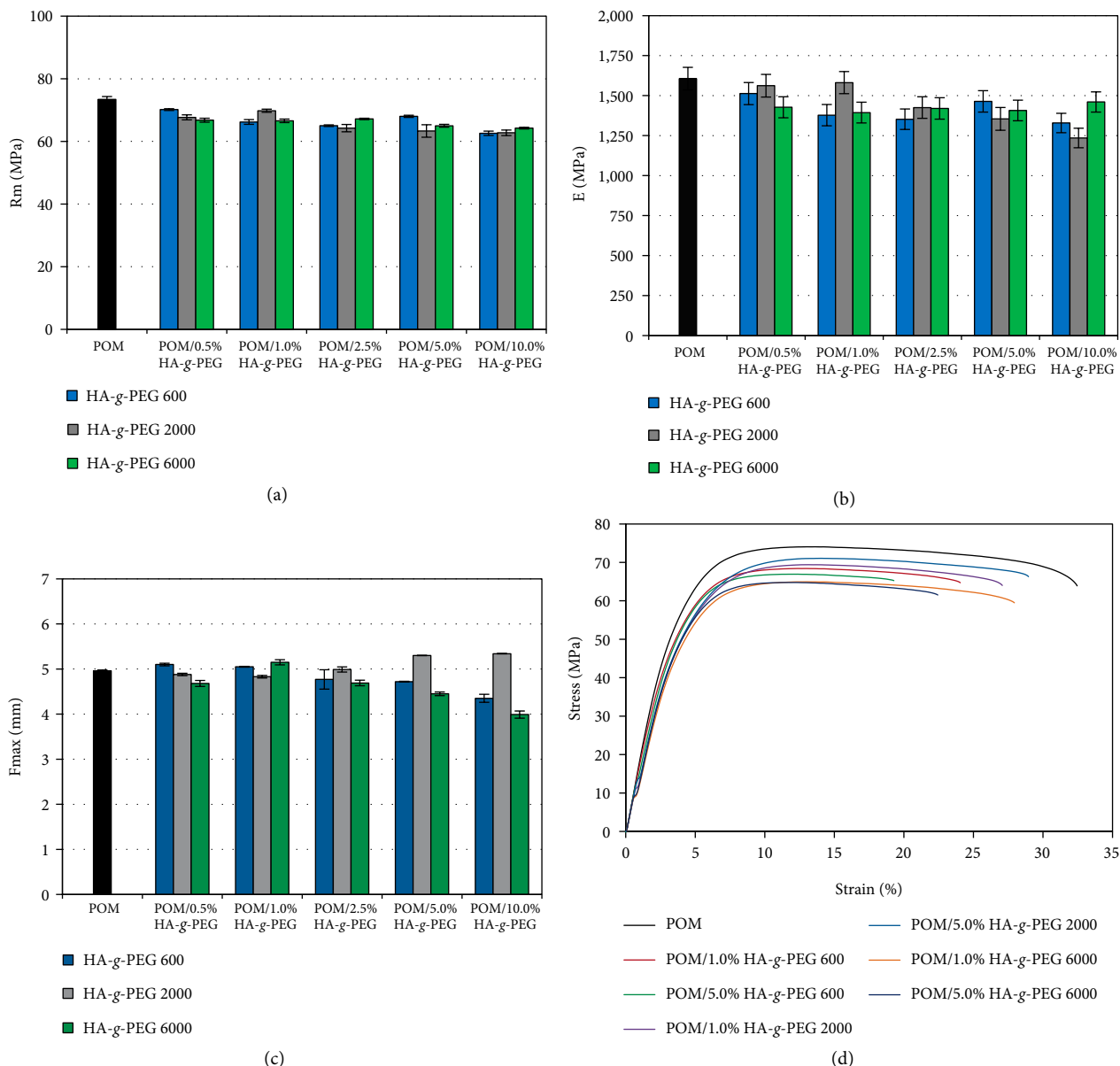


FIGURE 7: Tensile strength (a), Young modulus (b), elongation at break (c), and stress-strain curves (d) of POM/HA-g-PEG composites.

bending vibration peak appears at  $630\text{ cm}^{-1}$  [46]. No changes in the FTIR band position for all composites were detected. Additionally, for samples containing 5% HA-g-PEG, the  $602\text{ cm}^{-1}$  and  $567\text{ cm}^{-1}$  bands, arising from  $\text{PO}_4^{3-}$  asymmetric bending, were detected. As is known, the most common crystallographic form of POM is a hexagonal system, which consists of a 9/5 helical conformation, and it is the most stable form in terms of saving energy. In some specific conditions, POM can create orthorhombic crystals that are made up of 2/1 helical molecules. The typical hexagonal morphology of POM is usually a hybrid system which contains both folded chain crystals (FCC) and extended chain crystals (ECC). Although it is possible to separate bands from ECC and FCC based on IR spectra, these bands can overlap, and they may become indistinguishable. According to the literature [47], there are only two bands that are

strongly related to only one kind of crystal morphology: the band at  $1136\text{ cm}^{-1}$  that belongs only to FCC and band at  $891\text{ cm}^{-1}$  which is the vibrations of only an ECC structure. The other bands ( $1236\text{ cm}^{-1}$ ,  $1089\text{ cm}^{-1}$ ,  $933\text{ cm}^{-1}$ , and  $630\text{ cm}^{-1}$ ) come from the vibrations of both FCC and ECC crystal structures.

**3.5. Mechanical Properties of POM/HA-g-PEG Composites.** The tensile mechanical properties of POM/HA-g-PEG composites are presented in Figure 7. The tensile strength of the POM composites was slightly reduced with increasing HA-g-PEG.

The tensile strength (Figure 7(a)) decreased from 4.0% (1% HA-g-PEG 2000) to 16.3% (10% HA-g-PEG 2000) against the unmodified POM. The Young modulus (Figure 7(b)) of POM/HA-g-PEG composites also tends to decrease with increasing HA-g-PEG content. The samples containing from

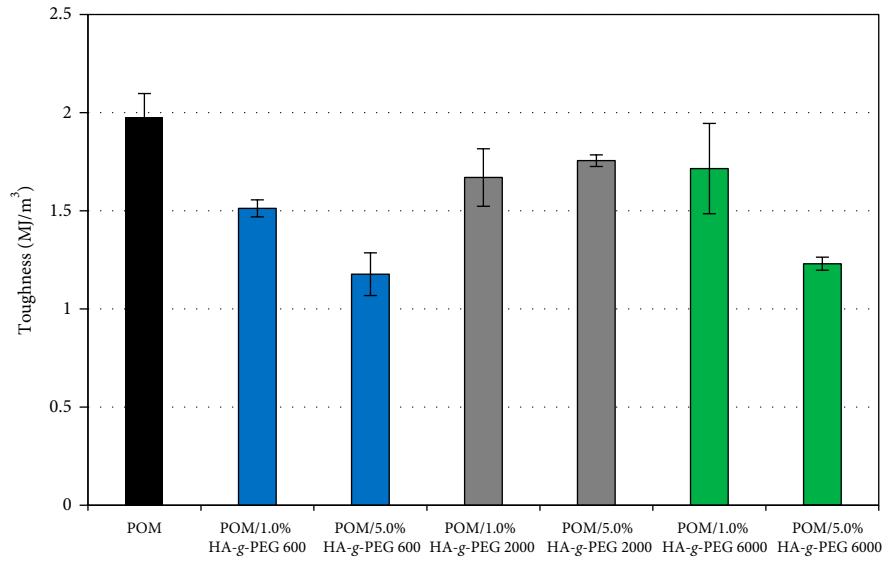


FIGURE 8: Toughness of POM/HA-g-PEG composites.

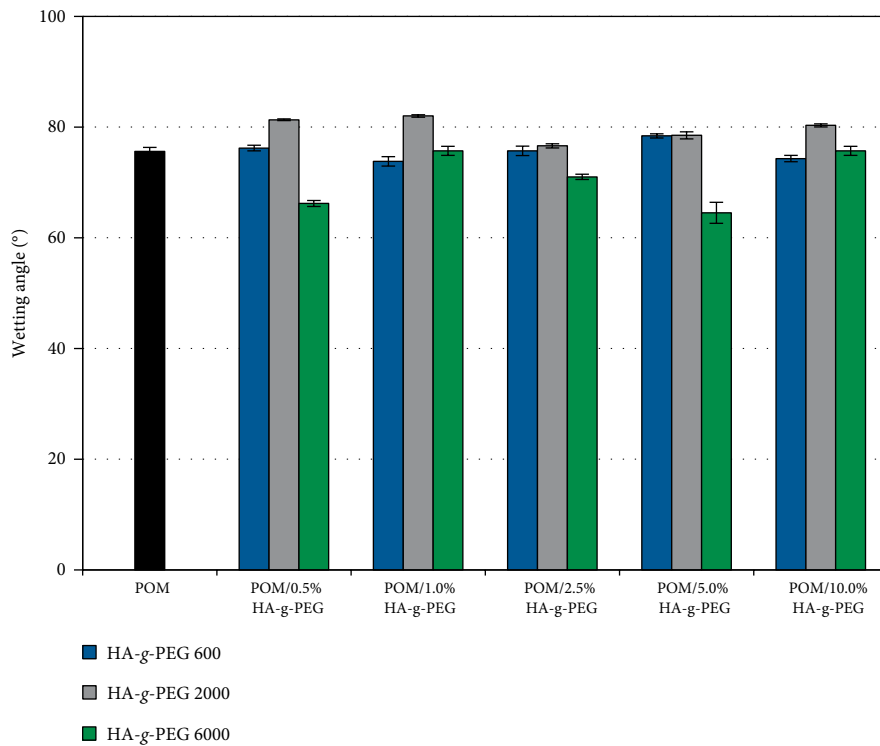


FIGURE 9: Wetting angle of POM/HA-g-PEG composites.

0.5–1% HA-g-PEG 2000 are an exception to this rule, and for these samples, the Young modulus is almost the same as for unmodified POM (the difference is from ~0.1–0.3%). This effect can be explained by the higher crystallinity of composites with lower additive content. The greatest loss in Young modulus, ~24.5 %, was detected for samples containing 10% HA-g-PEG 2000. There was no significant impact of HA-g-PEG on elongation at break up to 2.5% concentration of additive. HA-g-PEG 6000 contributed to the biggest decrease in

$F_{max}$  by decreasing the value of elongation at break by ~22% for a 10% HA-g-PEG 6000 load.

Compared to HA functionalized with PEG 2000 at a molar ratio of 2:2:1, better mechanical properties were found for HA functionalized with PEG 2000 at a molar ratio of 1:2:1. Based on the area under the stress-strain curves presented in Figure 7(d), the toughness of composites as the amount of energy a composite can absorb before fracture was calculated and is shown in Figure 8.

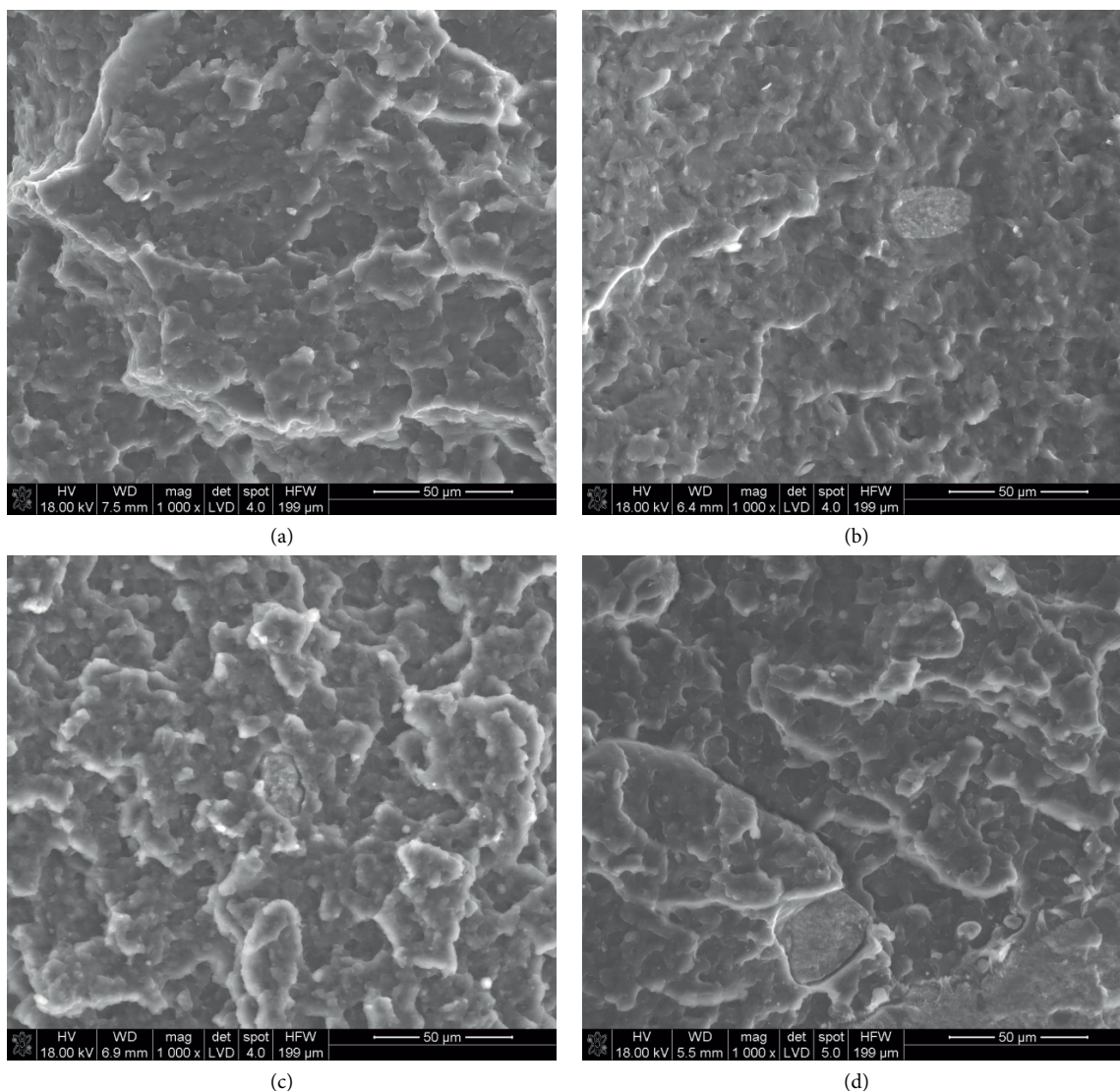


FIGURE 10: SEM images of cryogenically fractured surfaces of POM (a), POM/1.0% HA-g-PEG 600 (b), POM/1.0% HA-g-PEG 2000 (c), POM/1% HA-g-PEG 6000 (d) (mag.  $\times 1000$ ).

The addition of HA-g-PEG influenced the toughness of composites. Apart from HA-g-PEG 2000, the toughness of POM composites decreased with an increase in HA-g-PEG concentration. Therefore, the modified samples became more brittle; they broke much faster and the elongation was significantly smaller. Changes in mechanical properties of POM/HA-g-PEG composites are caused by changes in POM crystallinity due to the HA-g-PEG additive, which can disturb the formation of POM crystals, but can also act as a nucleating agent. Therefore, HA-g-PEG presence in POM can aid the growth of smaller crystals and strongly affect the kinetics of crystallization. There is also a strong relation between DSC studies and the mechanical test. Along with the degree of crystallinity increase, there is a proportional increase in elongation at break of composites.

**3.6. Wetting Properties of POM/HA-g-PEG Composites.** As POM is characterized by high lubricity, the HA-g-PEG influence on the wettability of POM surface was investigated.

The measurements of the wetting angle of POM/HA-g-PEG composites in Figure 9 show quite a significant influence of the hybrid additive on POM wettability.

The contact angle of unmodified POM was  $75.6^\circ \pm 1.5^\circ$ , which is a characteristic value for POM [46, 48]. Changes in POM wettability depend on the molar mass of PEG and its content in composites. For HA-g-PEG 600 there is only a minor decrease in POM wettability. For HA-g-PEG 2000, the biggest wettability increase, up to 8.5% higher than for pure POM for POM/1.0% HA-g-PEG 2000, is observed. By contrast, POM/HA-g-PEG 6000 composites are characterized by the lowest wettability, up to 14.7% lower than for unmodified POM.

Generally, a POM surface is considered as amphoteric (hydrophobic/hydrophilic), as the contact angle value is between  $45^\circ$  and  $90^\circ$  [49]. Some changes in POM wettability are caused by different configurations of POM chains. If the oxygen atoms in POM chains are exposed on the top of the surface, it becomes more hydrophilic. If oxygen atoms face

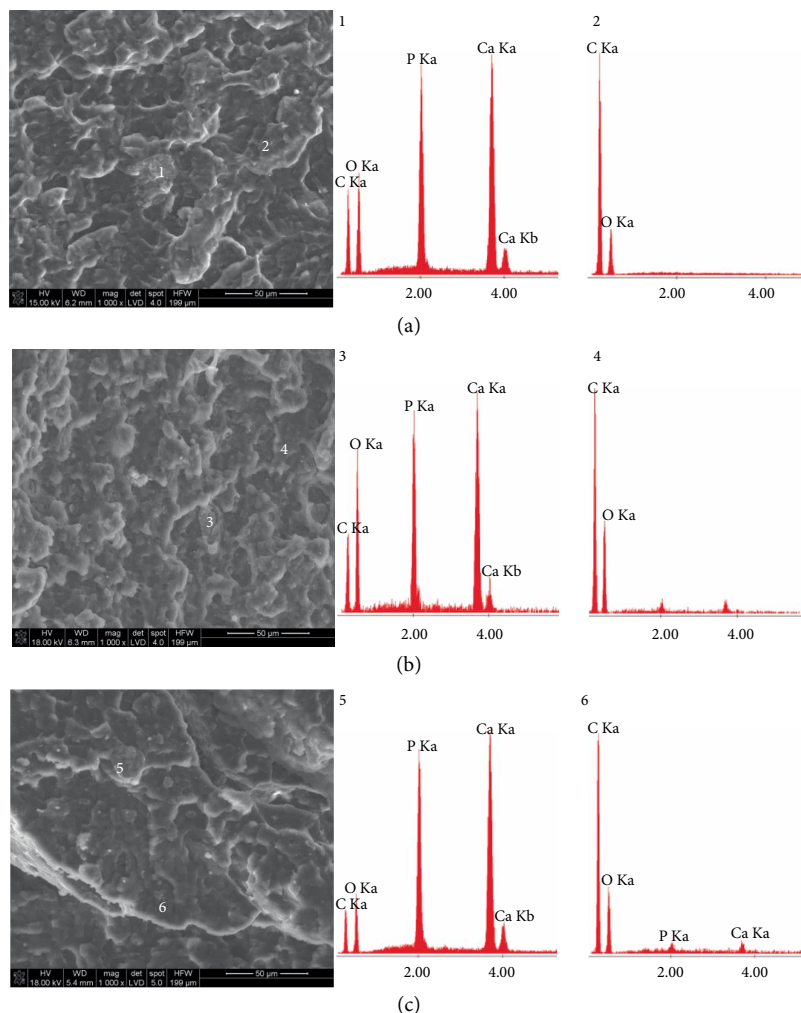


FIGURE 11: SEM/EDX analysis of POM/1.0% HA-g-PEG 600 (a), POM/1.0% HA-g-PEG 2000 (b), and POM/1.0% HA-g-PEG 6000 (c).

downward, the surface configuration is more hydrophobic [50]. This can cause different values of wettability on the POM surface. Furthermore, PEG presence in POM composites can affect the POM wettability. Although the POM  $-(\text{CH}_2-\text{O})_n-$  and PEG  $-(\text{CH}_2-\text{CH}_2-\text{O})_n-$  chemical formulas are very similar, PEG chains have the same configuration regardless of chain side. Therefore, the PEG surface is very consistent and the differences in PEG wettability are minimal. This makes PEG a hydrophobic, water-soluble polymer in contrast to the more hydrophobic, water-insoluble POM. Therefore, PEG acts as an extra lubricant for POM composites by improving the hydrophilicity of their surfaces just as HA does [51]. Thus, some increase in POM-based composite wettability can be associated with changes in the POM chain arrangement due to an HA-g-PEG presence, as well as being caused by the presence of PEG itself.

**3.7. SEM/EDX Analysis of Cryogenically Fractured Surfaces of POM/HA-g-PEG Composites.** SEM micrographs of cryogenically fractured surfaces of POM and POM/1.0% HA-g-PEG composites are presented in Figure 10.

HA-g-PEG particles ranged in size 25–35  $\mu\text{m}$ . A tight connection between the POM matrix and all HA-g-PEG

particles is observed. The composites can be treated as a heterogeneous compatible inorganic–organic mixture. For PEG-grafted HA particles with a higher molar mass of PEG, the POM surface became rougher and more cavities are found in the SEM micrographs. This effect is strongly associated with changes in the crystallinity of POM composites that was confirmed by DSC analysis (see Table 4). Mechanical studies also confirmed that the samples became more brittle when the molar mass of PEG in an HA-g-PEG system increased. Apart from the SEM study, a single point EDX analysis of POM/HA-g-PEG composites was performed and the results are presented in Figure 11. The EDX spectra of POM (2, 4, 6) exhibit peaks for only C and O, which are the major components of POM. For the HA-g-PEG particles (1, 3, 5), a peak for P and two peaks for Ca that come from HA are also observed. The intensity of oxygen bands in comparison to carbon peaks is also much higher than for pure POM.

**3.8. SEM/EDX Analysis of the Surface of POM/HA-g-PEG Composites after Incubation in SBF (3 Weeks).** The surface morphology of POM/HA-g-PEG composites after three

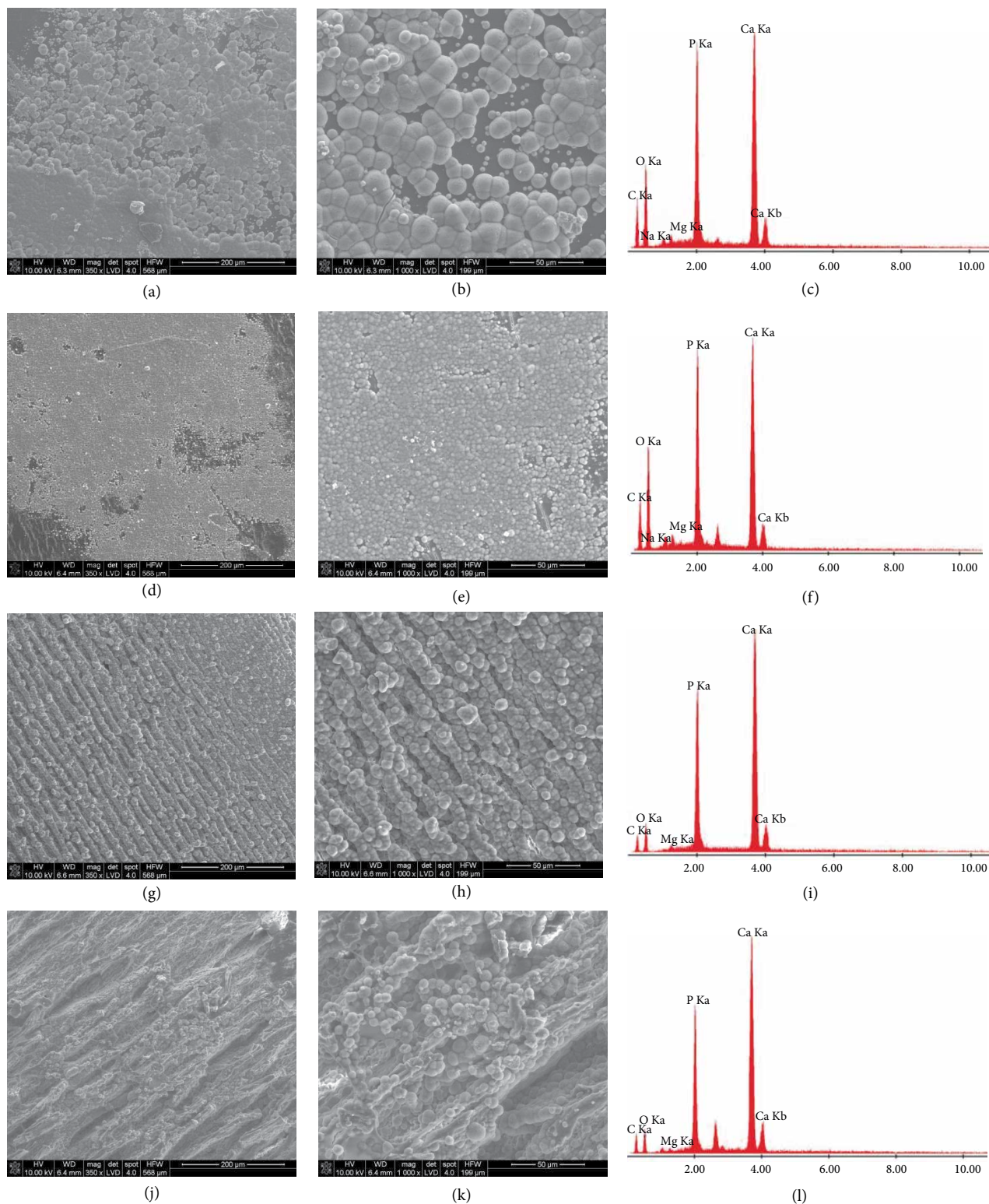


FIGURE 12: SEM/EDX results of POM/HA-g-PEG composites after incubation in SBF: (a–c) POM, (d–f) 5.0% HA-g-PEG 600, (g–i) 5.0% HA-g-PEG 2000, and (j–l) 5.0% HA-g-PEG 6000.

weeks immersion in SBF was examined by SEM/EDX and is presented in Figure 12. Unmodified POM is a bioinert material after incorporation to human body, but its bioactivity can be -improved by the incorporation of bioactive compounds like

HA. In our previous work it was found that the possibility of incorporation of higher amounts of HA to POM matrix is limited by the degradation of POM matrix that also limits bioactivity enhancement [22]. After HA functionalization no

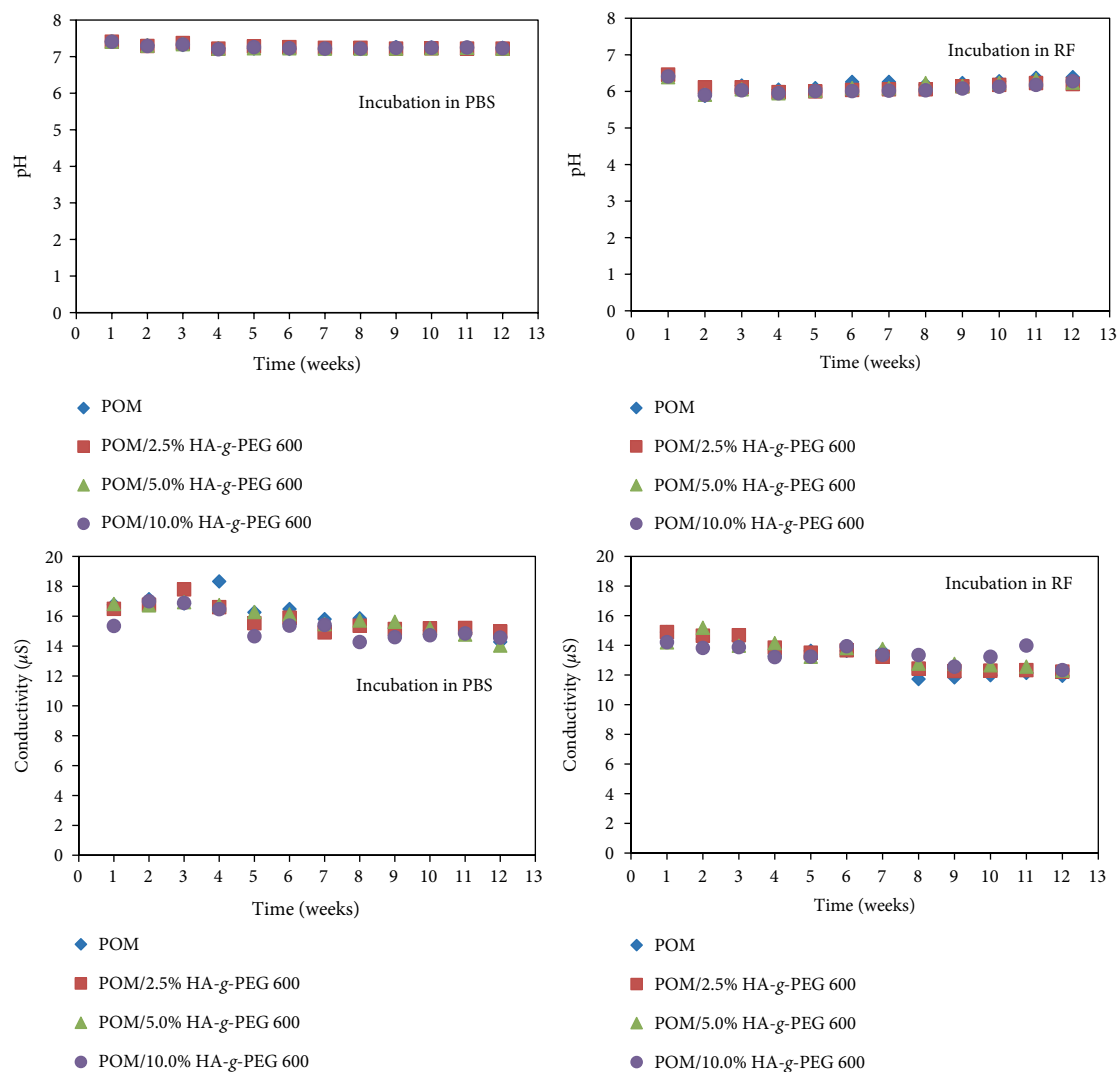


FIGURE 13: pH and conductivity changes of PBS and RF solutions as a function of incubation time of pristine POM and POM/HA-g-PEG 600 samples.

TABLE 5: EDX chemical ratio of Ca/P of apatite on the surface of POM/HA-g-PEG composites.

Sample	Ca/P ratio	
	at. %	wt. %
POM	1.52	1.96
POM/5.0% HA-g-PEG 600	1.47	1.90
POM/5.0% HA-g-PEG 2000	1.83	2.37
POM/5.0% HA-g-PEG 6000	2.03	2.63

POM degradation during processing was observed even for 10 wt. % of HA. As it can be seen incorporation of such relatively large amount of HA leads to significant improvement of POM bioactivity via formation of continuous layer of apatites. The Ca/P ratio (wt. % and at. %) of formed apatite layers was determined using EDX analysis and correlated in Table 5.

Results show that for pure POM (Figures 12(a)–12(c)) a single, discontinuous layer of apatite was formed on the POM surface. Well-formed, spherical microcrystallites of apatite,

up to  $20\mu\text{m}$  in diameter, with Ca/P ratio of 1.52 at. % (1.96 wt. %) were crystallized on the pristine POM surface. The surface of POM/5.0% HA-g-PEG 600 composite (Figures 12(d)–12(e)) was covered with fine apatite crystals, below  $5\mu\text{m}$  in diameter. The POM/HA-g-PEG composite surface was still not completely covered by the single layer of close-grained apatite crystals. The Ca/P ratio for apatite on the POM/ HA-g-PEG 600 composite decreased to 1.47 at. % (1.90 wt. %). In the POM/5.0% HA-g-PEG 2000 composite (Figures 12(g)–12(i)), the formation of a thick apatite multi-layer was observed. The apatite particles had a characteristic cauliflower-like morphology and they formed long, parallel rows. The most non-homogeneous microstructure of apatite was observed for POM/5.0% HA-g-PEG 6000. The apatite crystals differed in size and were not evenly deployed on the composite surface.

The addition of HA-g-PEG strongly improved apatite formation on the POM/HA-g-PEG composites along with an increase in the molar mass of PEG; however, the formed apatite became less stoichiometric.

TABLE 6: The mass of POM and POM/HA-g-PEG 600 samples before and after incubation in PBS and RF.

Sample	Mass [g]					
	Before incubation		After incubation		Mass change [g]	
	PBS	RF	PBS	RF	PBS	RF
POM	0.9403	0.8501	0.9398	0.8501	0.0005	0.0000
POM/2.5% HA-g-PEG 600	0.8839	0.9078	0.8834	0.9067	0.0005	0.0011
POM/5.0% HA-g-PEG 600	0.9529	0.8905	0.9529	0.8903	0.0000	0.0002
POM/10.0% HA-g-PEG 600	0.9606	0.9303	0.9601	0.9297	0.0005	0.0006

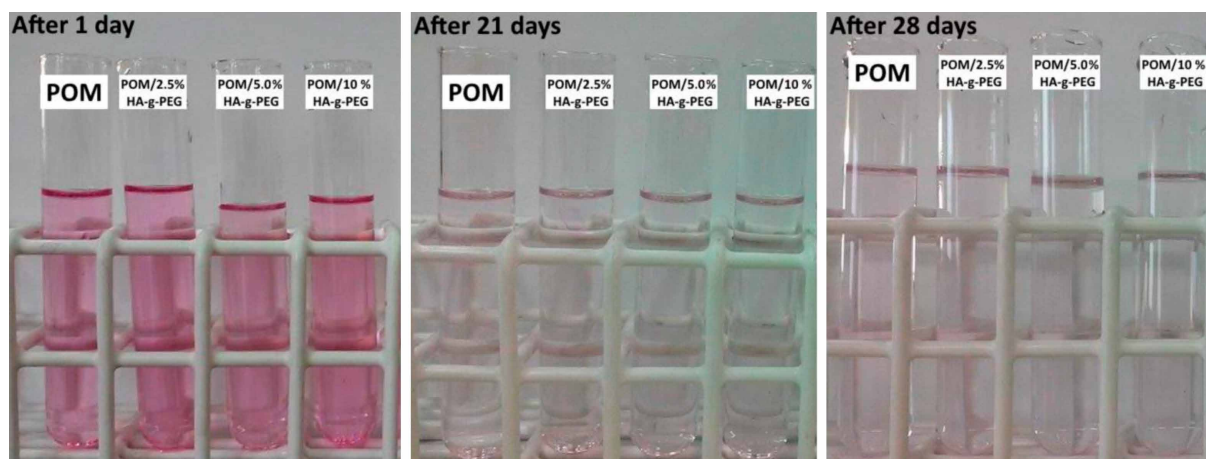


FIGURE 14: Colorimetric assay of formaldehyde release from POM/HA-g-PEG 600 composites after 1, 21, and 28 days.

**3.9. In Vitro Chemical Stability of POM/HA-g-PEG 600 Composites during a 3-month Incubation.** The *in vitro* chemical stability of POM/HA-g-PEG 600 composites was assessed by measurement of changes in pH and conductivity of PBS and Ringer's fluid during a three-month incubation at 37°C. Figure 13 shows that there were no significant changes in pH for both solutions; a minor decrease in the conductivity was detected. Samples containing 2.5%, 5.0% and even 10.0% of HA-g-PEG additives showed similar behaviour to unmodified POM. Moreover, the mass of all samples (Table 6), before and after incubation remained practically unchanged. These observations proved that both the POM matrix and HA-g-PEG 600 additive show good *in vitro* stability.

**3.10. Schiff Test Results for Formaldehyde Release from POM/HA-g-PEG 600 Composites.** A four-week dynamic incubation (37°C, distilled water) was conducted in order to assess the amount of formaldehyde released from POM/HA-g-PEG 600 composites in the Schiff test. Formaldehyde presence in the filtrates after 1, 21, and 28 days was determined using Schiff's reagent and the results are shown in Figure 14.

After one day of incubation of POM/HA-g-PEG 600 samples, there were no visible changes in the shade of pink in filtrates from composites containing different amount of HA-g-PEG 600. Furthermore, after 21 days of incubation, the colour of filtrates from samples containing 5.0% and 10.0% of HA-g-PEG 600 was nearly transparent. This indicates that the concentration of formaldehyde in these filtrates was less than 3 ppm. Moreover, it proved that incorporation of HA-g-PEG

600 into the POM matrix improved the thermal stability of POM. In addition, the significant amount of HA in the HA-g-PEG system improves the biocompatibility of POM intended for application as long-term bone implants.

#### 4. Conclusions

In this work, three different HA-g-PEG hybrid fillers, made from PEG with a molar mass of 600, 2000, or 6000 that was grafted on the HA surface using HDI as a coupling agent, were successfully introduced into POM matrix by melt processing methods. The highest increase in melting point and crystallinity was detected for POM/1.0% HA-g-PEG 600, which suggests that HA-g-PEG filler acts as a nucleating agent in POM. For a higher concentration of HA-g-PEG (5%) the POM crystallization process is disturbed, and a strong recrystallization effect is observed. Changes in the crystallinity of POM-based composites transfer to fractional decreases in the mechanical properties of these materials, such as (tensile strength, elongation at break, and Young's modulus). However, no phase shift in the XRD spectra of POM/HA-g-PEG composites in comparison to pure POM suggests that HA-g-PEG additive does not alter the hexagonal form of POM crystallites. The *in vitro* studies proved that incorporation of HA-g-PEG to a POM matrix improved bioactivity of the POM composites along with a PEG molar mass increase. Moreover, both the POM matrix and HA-g-PEG additive indicate very good *in vitro* chemical stability. Schiff's test confirmed the very low level of formaldehyde released from all POM/HA-g-PEG

composites and that all formaldehyde residue that comes from the POM processing was rinsed off the composites during the incubation. Moreover, there was no trace of new formaldehyde, which confirmed the good stability of all POM composites during the two-week incubation time.

## Data Availability

All data used to support the findings of this study are included within the article.

## Conflicts of Interest

The authors declare that they have no conflicts of interest.

## Acknowledgments

The authors are grateful to the Polish National Science Centre for financial support under the Contract No. UMO-2016/21/B/ST8/00449.

## References

- [1] A. K. Bledzki, A. A. Mamun, and M. Feldmann, "Polyoxymethylene composites with natural and cellulose fibres: toughness and heat deflection temperature," *Composites Science and Technology*, vol. 72, no. 15, pp. 1870–1874, 2012.
- [2] L. Guo, X. Xu, Y. Zhang, and Z. Zhang, "Effect of functionalized nanosilica on properties of polyoxymethylene-matrix nanocomposites," *Polymer Composites*, vol. 35, no. 1, pp. 127–136, 2014.
- [3] S. Lüftl, P. M. Visakh, and S. Chandran, *Polyoxymethylene Handbook: Structure, Properties, Applications and their Nanocomposites*, Wiley, 2014.
- [4] S. Lüftl, V. M. Archodoulaki, and S. Seidler, "Thermal-oxidative induced degradation behaviour of polyoxymethylene (POM) copolymer detected by TGA/MS," *Polymer Degradation and Stability*, vol. 91, no. 3, pp. 464–471, 2006.
- [5] L. W. McKeen, "3-polyether plastics," *The Effect of Temperature and Other Factors on Plastics and Elastomers*, Oxford: William Andrew Publishing, pp. 91–142, 3rd edition, 2014.
- [6] S. Lüftl, V. M. Archodoulaki, M. Glantschnig, and S. Seidler, "Influence of coloration on initial material properties and on thermooxidative ageing of a polyoxymethylene copolymer," *Journal of Materials Science*, vol. 42, no. 4, pp. 1351–1359, 2007.
- [7] V.-M. Archodoulaki, T. Koch, S. Lüftl, S. Seidler, and R. Stoiber, "Correlation between molar mass and thermal/mechanical properties of polyoxymethylene (POM) copolymers," MoDeSt 2010; Athens, Greece.
- [8] K. Pielichowska, "Polyacetals," *Plastics Engineering*, CRC Press pp. 193–249, 2nd edition, 2015, Handbook of Thermoplastics.
- [9] Y. Wang, W. Zhao, X. Wang, and D. Wu, "Preparation, mechanical properties and microstructure of polyoxymethylene fiber through melt spinning and hot drawing by using injection-molding grade resins," *Fibers and Polymers*, vol. 17, no. 9, pp. 1464–1474, 2016.
- [10] H. Asadollahi-yazdi, M. Shariati, A. Imam, and M. Ghatee, "Investigating the mechanical properties of layered graphene/polyoxymethylene nanocomposites prepared by the spray method," *Journal of Composite Materials*, vol. 51, no. 21, pp. 3053–3064, 2017.
- [11] K. Pielichowska, D. M. Bielinski, M. Dworak, E. Kilian, B. Macherzyńska, and S. Blazewicz, "The influence of nanohydroxyapatite on the thermal, mechanical and tribological properties of polyoxymethylene nanocomposites," *International Journal of Polymer Science*, vol. 2017, pp. 1–11, 2017.
- [12] Z.-Y. Wang, Y. Liu, and Q. Wang, "Flame retardant polyoxymethylene with aluminium hydroxide/melamine/novolac resin synergistic system," *Polymer Degradation and Stability*, vol. 95, no. 6, pp. 945–954, 2010.
- [13] V. M. Archodoulaki, S. Lüftl, and S. Seidler, "Stabiliser consumption of polyoxymethylene investigated by means of the pressure oxidative induction time method," *Polymer Testing*, vol. 27, no. 2, pp. 234–242, 2008.
- [14] R. P. Kusy and J. Q. Whitley, "Degradation of plastic polyoxymethylene brackets and the subsequent release of toxic formaldehyde," *American Journal of Orthodontics and Dentofacial Orthopedics*, vol. 127, no. 4, pp. 420–427, 2005.
- [15] Anon, "UV degradation & stabilization of polymers & rubbers," *Handbook of UV Degradation and Stabilization*, ChemTec Publishing, pp. 177–292, 2nd edition, 2015.
- [16] E. Richaud, "Polyoxymethylene additives," *Polyoxymethylene Handbook*, John Wiley & Sons, Inc., pp. 53–105, 2014.
- [17] Y. Hu, X. Zheng, and L. Ye, "Synergistic thermal stabilization effect of polyamide/melamine on polyoxymethylene," *Journal of Applied Polymer Science*, vol. 97, no. 6, pp. 2387–2391, 2005.
- [18] S. Wacharawichanant, S. Thongyai, A. Phutthaphan, and C. Eiamsam-ang, "Effect of particle sizes of zinc oxide on mechanical, thermal and morphological properties of polyoxymethylene/zinc oxide nanocomposites," *Polymer Testing*, vol. 27, no. 8, pp. 971–976, 2008.
- [19] X. Zhao, L. Gan, and L. Ye, "Structure and property of polyoxymethylene copolymerized with styrene oxide," *Journal of Polymer Research*, vol. 22, no. 1, 2015.
- [20] R. M. Meri, J. Zicans, A. Abele, T. Ivanova, and M. Kalnins, "Characterization of thermal destruction behavior of hybrid composites based on polyoxymethylene, ethylene-octene copolymer impact modifier and ZnO nanofiller," in *AIIP Conference Proceedings*, vol. 1736, no. 1, p. 020141 USA, 2016.
- [21] J. H. Dumbleton, "Delrin as a material for joint prosthesis – a review," American Society for Testing and Materials, Philadelphia, 1979, AST Corrosion and degradation of implant materials M Special Technical Publication.
- [22] K. Pielichowska, A. Szczygielska, and E. Spasówka, "Preparation and characterization of polyoxymethylene-copolymer/hydroxyapatite nanocomposites for long-term bone implants," *Polymers for Advanced Technologies*, vol. 23, no. 8, pp. 1141–1150, 2012.
- [23] E. Bouyer, F. Gitzhofer, and M. I. Boulos, "Morphological study of hydroxyapatite nanocrystal suspension," *Journal of Materials Science: Materials in Medicine*, vol. 11, pp. 523–531, 2000.
- [24] Q. Liu, W. Guo, M. Yang, K. Wang, W. Liu, and F. Wu, "Release behavior of folic acid grafted hollow hydroxyapatite as drug carrier," *Advances in Polymer Technology*, vol. 2019, pp. 1–9, 2019.
- [25] K. Pielichowska, K. Król, and T. M. Majka, "Polyoxymethylene-copolymer based composites with PEG-grafted hydroxyapatite with improved thermal stability," *Thermochimica Acta*, vol. 633, pp. 98–107, 2016.

- [26] K. Pielichowska, "Thermooxidative degradation of polyoxymethylene homo- and copolymer nanocomposites with hydroxyapatite: Kinetic and thermoanalytical study," *Thermochimica Acta*, vol. 600, pp. 7–19, 2015.
- [27] G. M. Poralan, J. E. Gambe, E. M. Alcántara, and R. M. Vequizo, "X-ray diffraction and infrared spectroscopy analyses on the crystallinity of engineered biological hydroxyapatite for medical application," *IOP Conference Series Materials Science and Engineering*, vol. 79, no. 1, p. 012028, 2015.
- [28] R. Barabás, M. Czikó, I. Dékány, L. Bizo, and E. S. Bogya, "Comparative study of particle size analysis of hydroxyapatite-based nanomaterials," *Chemical Papers*, vol. 67, no. 11, 2013.
- [29] <http://download.springer.com/static/pdf/98/bbm%253A978-3-540-26360-9%252F1.pdf?auth66=1426842262fe2f3201d3bfe0d62667e8e9f849fa02&ext=pdf>.
- [30] M. Fuensanta, J. A. Jofre-Reche, F. Rodríguez-Llansola, V. Costa, J. I. Iglesias, and J. M. Martín-Martínez, "Structural characterization of polyurethane ureas and waterborne polyurethane urea dispersions made with mixtures of polyester polyol and polycarbonate diol," *Progress in Organic Coatings*, vol. 112, pp. 141–152, 2017.
- [31] A. Güney and N. Hasirci, "Properties and phase segregation of crosslinked PCL-based polyurethanes," *Journal of Applied Polymer Science*, vol. 131, no. 1, pp. n/a–n/a, 2014.
- [32] M. A. Javaid, R. A. Khera, K. M. Zia, K. Saito, I. A. Bhatti, and M. Asghar, "Synthesis and characterization of chitosan modified polyurethane bio-nanocomposites with biomedical potential," *International Journal of Biological Macromolecules*, vol. 115, pp. 375–384, 2018.
- [33] F. E. Bailey and J. V. Koleske, *Poly(ethylene oxide)*, Academic Press, 1976.
- [34] A. Rapacz-Kmita, C. Paluszkiwicz, A. Ślósarczyk, and Z. Paszkiewicz, "FTIR and XRD investigations on the thermal stability of hydroxyapatite during hot pressing and pressureless sintering processes," *Journal of Molecular Structure*, vol. 747, pp. 653–656, 2005.
- [35] B. R. Barrioni, S. M. de Carvalho, R. L. Oréface, A. A. R. de Oliveira, and M. D. M. Pereira, "Synthesis and characterization of biodegradable polyurethane films based on HDI with hydrolyzable crosslinked bonds and a homogeneous structure for biomedical applications," *Materials Science and Engineering: C*, vol. 52, pp. 22–30, 2015.
- [36] M. S. M. Arsad, P. M. Lee, and L. Kong Hung, "Synthesis and characterization of hydroxyapatite nanoparticles and  $\beta$ -TCP particles," *International Conference on Biotechnology and Food Science*, 2011.
- [37] Z. Y. Li, W. M. Lam, C. Yang et al., "Chemical composition, crystal size and lattice structural changes after incorporation of strontium into biomimetic apatite," *Biomaterials*, vol. 28, no. 7, pp. 1452–1460, 2007.
- [38] T. Tsuchida, J. Kubo, T. Yoshioka, S. Sakuma, T. Takeguchi, and W. Ueda, "Reaction of ethanol over hydroxyapatite affected by Ca/P ratio of catalyst," *Journal of Catalysis*, vol. 259, no. 2, pp. 183–189, 2008.
- [39] C. L. Kibby and W. K. Hall, "Dehydrogenation of alcohols and hydrogen transfer from alcohols to ketones over hydroxyapatite catalysts," *Journal of Catalysis*, vol. 31, no. 1, pp. 65–73, 1973.
- [40] S. J. Joris and C. H. Amberg, "Nature of deficiency in nonstoichiometric hydroxyapatites. I. Catalytic activity of calcium and strontium hydroxyapatites," *The Journal of Physical Chemistry*, vol. 75, no. 20, pp. 3167–3171, 1971.
- [41] Y. Matsumura and J. B. Moffat, "Methanol adsorption and dehydrogenation over stoichiometric and non-stoichiometric hydroxyapatite catalysts," *Journal of the Chemical Society, Faraday Transactions*, vol. 92, no. 11, pp. 1981–1984, 1996.
- [42] F. Barroso-Bujans, F. Fernandez-Alonso, J. A. Pomposo, S. Cervený, A. Alegría, and J. Colmenero, "Macromolecular structure and vibrational dynamics of confined poly(ethylene oxide): from subnanometer 2D-intercalation into graphite oxide to surface adsorption onto graphene sheets," *ACS Macro Letters*, vol. 1, no. 5, pp. 550–554, 2012.
- [43] K. Pielichowska, J. Bieda, and P. Szatkowski, "Polyurethane/graphite nano-platelet composites for thermal energy storage," *Renewable Energy*, vol. 91, pp. 456–465, 2016.
- [44] X. Liu, S. Bai, M. Nie, and Q. Wang, "Effect of blend composition on crystallization behavior of polyoxymethylene/poly(ethylene oxide) crystalline/crystalline blends," *Journal of Polymer Research*, vol. 19, no. 1, Article ID 9787, 2011.
- [45] M. Raimo, "Structure and morphology of polyoxymethylene," *Polyoxymethylene Handbook*, John Wiley & Sons, Inc. pp. 163–91, 2014.
- [46] M. S. Rahman, U. Shaislamov, J.-K. Yang et al., "Effects of electron beam irradiation on tribological and physico-chemical properties of polyoxymethylene copolymer (POM-C)," *Nuclear Instruments and Methods in Physics Research Section B: Beam Interactions with Materials and Atoms*, vol. 387, pp. 54–62, 2016.
- [47] Y. Li, T. Zhou, Z. Chen, J. Hui, L. Li, and A. Zhang, "Non-isothermal crystallization process of polyoxymethylene studied by two-dimensional correlation infrared spectroscopy," *Polymer*, vol. 52, no. 9, pp. 2059–2069, 2011.
- [48] A. J. Jose and M. Alagar, "Development and characterization of organoclay-filled polyoxymethylene nanocomposites for high performance applications," *Polymer Composites*, vol. 32, no. 9, pp. 1315–1324, 2011.
- [49] A. Abdelbary, *Wear of Polymers and Composites*, Elsevier, pp. 133–158, 2015.
- [50] H. Yasuda, *Magneto Luminous Chemical Vapor Deposition*, CRC Press, 2011.
- [51] T. G. Tihan, M. D. Ionita, R. G. Popescu, and D. Iordachescu, "Effect of hydrophilic–hydrophobic balance on biocompatibility of poly(methyl methacrylate) (PMMA)–hydroxyapatite (HA) composites," *Materials Chemistry and Physics*, vol. 118, no. 2–3, pp. 265–269, 2009.

